Bimodal distribution of neon nanobubbles in aluminum

R. S. Dhaka and S. R. Barman*
UGC-DAE Consortium for Scientific Research, Khandwa Road, Indore 452001, Madhya Pradesh, India
(Received 12 November 2008; revised manuscript received 26 January 2009; published 6 March 2009)

Ne 1*s* core-level photoelectron spectra from Ne nanobubbles implanted in aluminum exhibit two peaks whose binding energies and relative intensities change with implantation energy, isochronal annealing, and sputtering. These changes in the core-level spectra are manifestations of the nanometer size of the bubbles since the screening of the photohole by the Al conduction electrons depends on the bubble size. Existence of a bimodal depth and size distribution of Ne nanobubbles is demonstrated in this work: smaller bubbles of about 4 Å in radius are formed close to the Al(111) surface while the larger sized bubbles of 20 Å in radius exist deeper below in the beneath subsurface region. A general relation between the radius of the rare-gas bubbles and their core-level binding energies is established.

DOI: 10.1103/PhysRevB.79.125409 PACS number(s): 82.80.Pv, 61.80.Jh, 79.60.−i

I. INTRODUCTION

The study of low dimensional systems is a subject of current research interest because of their intriguing physical properties and the promise for new technology. Here, we study a nearly zero dimensional quantum dot-like system that is formed by a complex process of self-assembly in a metal matrix. These are rare-gas bubbles of nanometer size that are produced by implantation of rare-gas atoms in Al.[1–10] The nanobubbles exhibit fascinating properties: it has been reported that overpressurized rare-gas bubbles exist in solid state at room temperature.[1] Solid Ar bubbles have been observed to melt at 730 K.[2] With change in bubble size, transition between ordered solid and disordered fluid phases has been observed in Xe.[3] Evidence of electron interference between the Al surface and the subsurface Ar bubbles has been established by scanning tunneling microscopy.[4] Theoretical studies relate the bubble formation to the repulsive pseudopotential between the rare-gas atoms and the surrounding Al conduction electrons.[5] Ne nanobubbles in Al have been studied by transmission electron microscopy and electron energy loss spectroscopy, and bubbles of about 13 Å in radius were found to be in fluid state.[1]

Rare-gas atoms in nearly-free-electron metals provide an ideal system for studying the response of the conduction electrons to the photohole generated in the photoemission final state.[8,9] A decrease in the core-level binding energy (BE) of the implanted rare-gas atoms with respect to their gas phase BE was related to the relaxation energy associated with the screening of the core hole by host-metal electrons.[11–13] In Refs. 8 and 9, we established that the screening by the Al conduction electrons depends on the size of the Ar and Xe bubbles. In this work, we apply this concept to Ne bubbles in Al. Ne being lighter than Ar or Xe, their mobility and penetration depth would be higher, and this might result in a different behavior. Indeed, we find a clear signature of bimodal distribution of the Ne bubble size, which has not been observed earlier for Ar or Xe.[3,4,8,9]

II. EXPERIMENTAL METHOD

X-ray photoelectron spectroscopy (XPS) has been performed by using an electron energy analyzer from Specs GmbH, Germany. The overall energy resolution was 0.8 eV using 20 eV analyzer pass energy. The base pressure of the chamber was 4×10^{-11} mbar. Al(111) was cleaned by repeated cycles of sputtering using 1–2 keV Ne^+ and subsequent annealing at 723 K to regenerate surface order and to remove the Ne implanted during sputtering.[14] The surface crystallinity was confirmed by a sharp 1×1 low energy electron-diffraction pattern that is characteristic of Al(111).[9] Absence of oxygen and carbon contaminations as well as any remaining Ne implanted during sputtering was checked by XPS after annealing the specimen to 723 K. Subsequently, Ne^+ ions were implanted *in situ* in normal-incidence geometry at pressure of about 1×10^{-5} mbar for different durations at temperatures somewhat higher than room temperature ($\approx$340 K). One monolayer (ML) fluence of Ne atoms hitting the Al surface is defined to be equal to the number of Al atoms on the Al(111) surface (1.415×10^{15}).[9,15]

The Ne 1*s* core-level spectra have been fitted by using a least-squares error minimization routine based on the Levenberg-Marquardt algorithm[16] with two Doniach-Šunjić (DS) (Ref. 17) line shapes. The DS lines are characterized by the peak position, intensity, intrinsic lifetime broadening [half width at half maximum (HWHM) ($=\gamma$)], and the asymmetry parameter (α). α and γ have been taken to be the same for both lines. To avoid unphysical values of α and resulting problems with the convergence of the fitting routine, we constrained it to be greater than or equal to zero. γ is constrained to be $\geq$0.135 eV since this is the minimum value for Ne 1*s* measured with high resolution in the gas phase.[18] In order to account for the instrumental factors (i.e., the analyzer and the photon source related broadenings), the DS line shape has been convoluted with a Voigt function. This Voigt function can be regarded as the characteristic of the instrument, and is dependent on photon source and analyzer settings for the measurements. The parameters defining the Voigt function (for example, the Lorentzian and Gaussian broadenings) have been obtained from fitting of the Al 2*p* core-level spectrum of clean Al(111), for which the intrinsic lifetime broadening ($2\gamma=30$ meV) and $\alpha\,(=0.1)$ are known from high-resolution Al 2*p* core-level studies.[19] The Ne 1*s* spectra have been collected with the same analyzer settings and hence the same broadening parameters, as determined for clean Al 2*p*, were used. But the rare-gas core-level spectra could not be

fitted using the instrumental broadening parameters, and it was obvious that there is an extra broadening. So, both the Lorentzian and Gaussian broadening parameters were allowed to vary, and only the Gaussian parameter increased quite substantially from the instrumental value. Hence, it is clear that the Ne 1*s* core level has an extra component of Gaussian broadening over and above the instrument related Gaussian broadening. The full width at half maximum (FWHM) ($=w_g$) of this extra Gaussian was varied while the instrumental Gaussian broadening was kept fixed. w_g varied between 0.6–0.8 eV for the different Ne 1*s* spectra. It may be noted that the quality of the fitting is good, as depicted by the residual, which is within the statistical scatter of the experimental data for all cases.

III. RESULTS AND DISCUSSION

The Ne 1*s* core-level spectra in Fig. 1(a) exhibit two clear peaks. This is unexpected because an *s* level has no spin-orbit splitting and generally exhibits a single peak. We denote these peaks, separated by about 1.2 eV, as Ne $1s_A$ and $1s_B$. What is even more surprising is that the relative intensities of these peaks change with the implantation energy (E_i). The intensity of Ne $1s_A$ decreases while that of Ne $1s_B$ increases with E_i. For example, at E_i=0.3 keV, the $1s_A$:$1s_B$ intensity ratio is about 2 while at 5 keV it is 0.4 [inset of Fig. 1(a)]. The intensity ratio decreases sharply up to 3 keV.

The BE of Ne $1s_A$ at E_i=0.3 keV is 863.5 eV with respect to the Fermi level [lowest spectrum in Fig. 1(a)]. This is about 2.6 eV smaller in magnitude than the gas phase value.[20] On the other hand, Ne $1s_B$ has 1.3 eV lower BE compared to the gas phase. However, with different implantation conditions (E_i and fluence), BE shift of both Ne $1s_A$ and $1s_B$ peaks is observed. This is shown by the contour plots in Figs. 1(b) and 1(c), where ΔE_B is defined as the difference between the Ne 1*s* BE in the gas phase and for the bubble. The shift is also evident from the spectra in Fig. 1(a): both peaks shift by about 0.4 eV toward higher BE between 0.3 and 5 keV. The shift in BE with implantation conditions has also been observed for Ar and Xe nanobubbles in Al,[8,9] and its implication for Ne bubbles will be discussed later.

In order to understand the origin of the two peaks in the Ne 1*s* spectra, we note that the growth of rare-gas bubbles occur via thermally activated processes such as thermal vacancy absorption, migration, and coalescence of the bubbles.[21] So, we have studied the Ne nanobubbles implanted with E_i=1.5 keV, as a function of isochronal annealing temperature (T_A). With isochronal annealing, an overall increase in BE of about 0.4 eV is observed for both $1s_A$ and $1s_B$ [Fig. 2(a)], which indicates increase in bubble size due to the above mentioned thermally activated processes. This has also been observed earlier for Ar and Xe bubbles.[9,21] The overall Ne concentration (as defined in Ref. 9) decreases from about 1.3%–0.1% between 200 and 545 K [Fig. 2(c)], which also shows the increased mobility of Ne atoms at higher temperature that results in increased desorption rate. Most important is the significant change in the intensity ratio of the two Ne 1*s* peaks [Figs. 2(a) and 2(b)]. For $T_A \leq 440$ K, Ne $1s_A$ has higher intensity compared to $1s_B$. The intensity ratio is about 1.2 at 340 K, and shows a small decrease up to 440 K. However, above this temperature, the ratio decreases sharply and at 545 K, where Ne $1s_B$ is clearly more intense, it is about 0.5. Thus, it is evident that annealing influences the two Ne 1*s* peaks differently. The relative decrease in Ne $1s_A$ intensity with increasing T_A indicates that the corresponding Ne bubbles may be residing close below the surface (subsurface), and thus the desorption rate would be higher compared to the other species (Ne $1s_B$) that might occur deeper below (beneath subsurface).

Note that the above discussed origin of the double peak structure of Ne 1*s* also explains their relative intensity variation with E_i [inset of Fig. 1(a)]. We have calculated the mean implantation depth (d) using the Monte Carlo based [transport of ions through matter (TRIM)] method[22] considering Ne atoms impinging on Al in normal-incidence geometry. The results presented in Fig. 1(d) show that d increases with E_i, and similar behavior has been obtained earlier for Ar and Xe.[9] This implies that the number of Ne atoms in the subsurface region would be smaller than the beneath subsurface region for higher E_i. Thus, the intensity of the subsurface related Ne $1s_A$ peak decreases because more bubbles are formed in the beneath subsurface region at the expense of the subsurface bubbles. In the subsurface region, the probability of the Ne atoms diffusing out through the surface would be naturally larger than for the deeper lying bubbles. So the concentration is less and only a fraction of the Ne atoms will form bubbles of smaller size. The Ne concentration decreases as E_i decreases: from 4% at 5 keV to 0.05% at 0.3 keV [Fig. 1(e)].

Further evidence that Ne $1s_A$ is subsurface related comes from the following experiment: the Al surface with implanted Ne nanobubbles was sputtered using 0.5 keV Ar ions for a time period that would remove about 1 ML of Al. Surprisingly, *after* sputtering, Ne $1s_A$ decreases drastically while Ne $1s_B$ remains essentially unchanged (Fig. 3). This effect is clearly evident in Fig. 3, where implantation has been done with low E_i (=0.3 keV) so that most of the bubbles are formed in the subsurface region and Ne $1s_A$ is dominant *before* sputtering. Relative decrease in Ne $1s_A$ is also observed for other implantation conditions, such as E_i =1.5 and 3 keV. Thus, although Ar ion sputtering is intended to remove only one monolayer of Al, it causes a large decrease in the Ne $1s_A$ peak intensity. This indeed signifies that the Ne $1s_A$ related bubbles are formed close to the surface.

From the above discussion, a bimodal depth distribution of the Ne bubbles is evident. This observation is supported by previous theoretical studies by Busse *et al.*[15] They calculated the vacancy distribution created by 1 keV Ne and Xe bombardment on Al using molecular-dynamics (MD) simulation. The MD simulations showed that the ion bombardment locally melts the Al surface through formation of a thermal spike,[23] and the molten region recrystallizes after a few picoseconds and formation of adatoms and vacancies occur. Busse *et al.*[15] found that even though a slightly larger number of molten Al atoms are produced in Ne compared to Xe, for Ne the molten Al atoms cool faster than for Xe and this was related to the diffuse shape of the spike produced for Ne. Moreover, while the vacancy distribution produced by Xe is symmetric around mean depth, for Ne the first maxi-

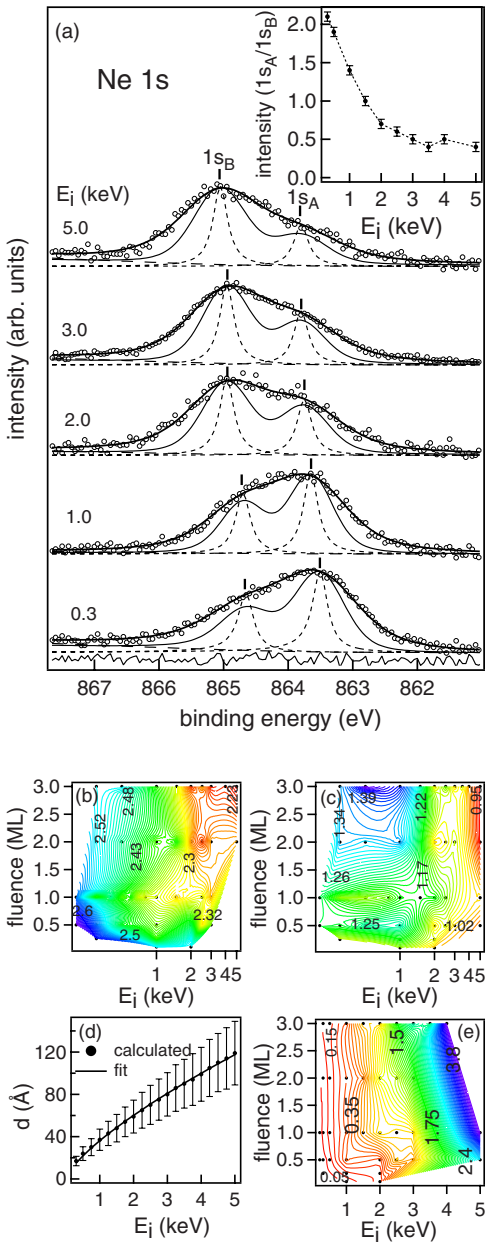

FIG. 1. (Color online) (a) Ne 1*s* core-level spectra (open circles) and the fitted curve (thick solid line) as a function of the implantation energy (E_i) for 3 ML fluence. The experimental spectra have been normalized to the same height. The deconvoluted DS line shape (short-dashed line), the spectral line shape including the Gaussian broadening (w_g) but excluding the instrumental broadening (thin solid line), and the inelastic Tougaard background (dot-dashed line) are shown. The spectra are staggered along the vertical axis. The residue for the 0.3 keV spectrum is shown in the bottom. The intensity ratio of Ne $1s_A$ and $1s_B$ is shown in the inset. ΔE_B variation in (b) Ne $1s_A$ and (c) Ne $1s_B$ with E_i and fluence. For $1s_A$ ($1s_B$), in the rainbow color scheme (gray scale), the violet (darkest) contour represents 2.6 (1.3) eV, while the red (lightest) contour is 2.2 (0.9) eV. (d) The calculated mean implantation depth (d) (filled circles) and the fitted curve (solid line); the bars show the straggle. (e) Concentration of implanted Ne in Al, where the violet contour represents 4% while the red is 0.05%. (b), (c), and (e) The dots in the contour plots show the different E_i and fluence combinations for which the experiments were performed.

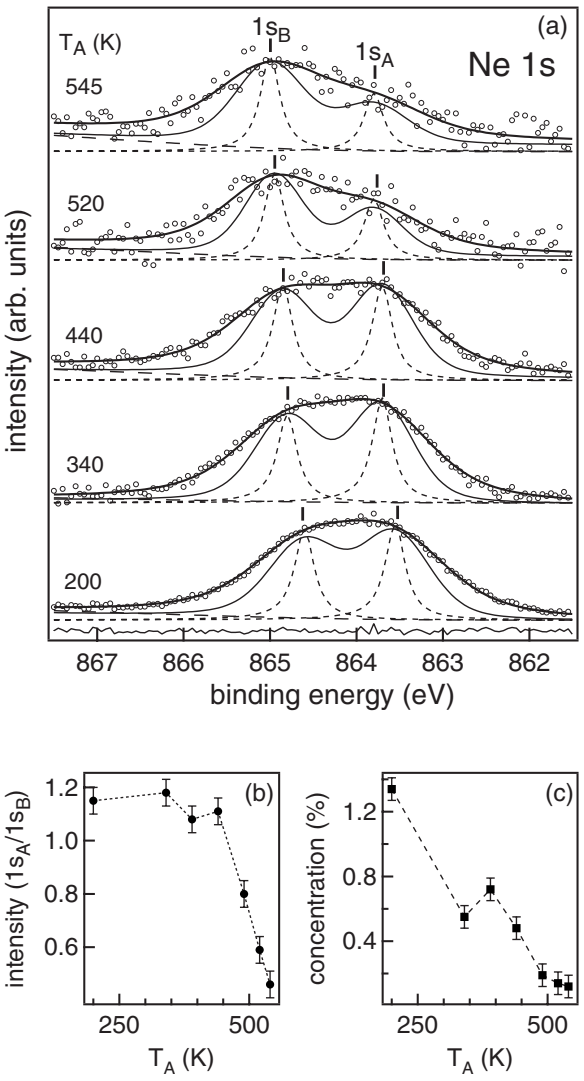

FIG. 2. (a) Ne 1*s* core-level spectra (open circles) normalized to same height and the fitted curve (thick solid line) as a function of T_A for the nanobubbles formed with E_i=1.5 keV and 1 ML fluence. The other line types have the same meaning as in Fig. 1(a). (b) The intensity ratio of $1s_A$ and $1s_B$, and (c) concentration of Ne.

mum is at the surface layer (see Fig. 10 of Ref. 15). A minimum in vacancy distribution was observed in the second layer that separated the two maxima of the vacancy distribution. The sputter yield was also found to be high for Ne. The physical explanation for the different behavior of Ne compared to Xe was related to the efficient energy transfer between Ne and Al atoms because of their similar masses, as a result of which the energy deposited in the surface region is high for Ne bombardment.[15]

The MD simulation considered individual ion impact events on Al, and thus did not study the bubble formation phenomenon. However, on the basis of existing MD results discussed above, we suggest that the bimodal depth distribution of vacancies is the origin of the bimodal depth distribution of the Ne bubbles since the vacancies are the likely nucleating points for bubble formation.[8] A large fraction of the bombarded Ne atoms after being implanted in Al would have sufficient energy to undergo diffusion, scattering, and

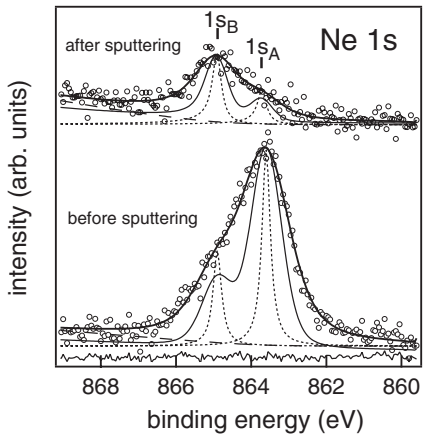

FIG. 3. Ne 1*s* core-level spectra (open circles) for bubbles (implanted with E_i=0.3 keV and fluence of 1 ML) *before* and *after* Ar ion sputtering. The line types have the same meaning as in Fig. 1(a).

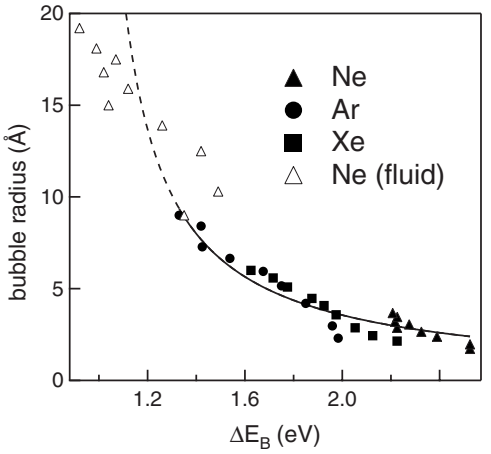

FIG. 4. Bubble radii of Ar, Xe, and Ne plotted as a function of ΔE_B. The bubbles in the solid state are represented by filled symbols. The fitted curve (line) for the solid bubbles is extrapolated as dashed line.

desorb out through the surface. Due to the efficient energy coupling between lighter Ne and Al,[15] Ne atoms that reach the surface will have less energy in an average than heavier Xe atoms. Thus, the probability that Ne would form bubbles nucleating at the vacancies would be larger compared to desorption by overcoming the surface binding energy. This explains the occurrence of bimodal depth distribution in Ne in contrast to Xe or Ar. Interestingly, bimodal distribution has been observed for He bubbles in metals under hot implantation conditions.[24]

Next, the reason for the large BE difference of 1.2 eV between $1s_A$ and $1s_B$ needs to be understood. As mentioned in Sec. I, in previous theoretical studies on implanted rare-gas atoms in metals, ΔE_B was related to the relaxation energy,[11–13] which arises because of the extra atomic screening by the metal conduction electrons. The relaxation energy was found to vary inversely with the effective radius of the implanted rare-gas atom.[9,12] The other factors on which the BE can depend are the intra-atomic relaxation effect, change in pressure, physical state of the rare-gas atoms, and dipole barrier at the bubble interface. Pressure change can shift the core levels but we showed through explicit calculations in Ref. 9 that pressure effects only the valence band and shallow levels but not the deep core levels such as Ar 2*p* (242.3 eV BE). Ne 1*s* is a deeper core level (BE≈864 eV) than Ar 2*p* and so change in pressure is highly unlikely to affect the BE. The intra-atomic relaxation, the physical state (solid or fluid), or the dipole barrier does not explain the systematic change in BE of Ne 1*s* with implantation conditions. The effect of the physical state (solid or fluid) on Ne 1*s* BE is discussed later.

In Refs. 8 and 9, we have shown that, as the size of the bubble increases, the extra atomic screening of the photohole by Al conduction electrons in the final state of photoemission becomes weaker and the rare-gas core-level BE increases. Thus, higher ΔE_B, i.e., lower BE would indicate smaller bubble size for Ne $1s_A$ compared to $1s_B$. We fit ΔE_B of Ne $1s_A$ with E_i using Eq. (2) of Ref. 8, which gives n =0.27. Assuming that for smallest E_i the bubble radius (R_0) corresponds to the Van der Waals radius of Ne, we find R to be about 4 Å at 5 keV. To calculate the width of the size distribution the following may be noted: since the BE of the Ne 1*s* core level depends on the bubble size, a symmetrical distribution of bubble size will result in a symmetrical distribution of the core-level peak positions around the mean position. Such symmetrical distribution of the rare-gas bubbles in Al has been reported from transmission electron microscopy studies for Ar, Xe, and He.[2,7,25,26] From our fitting, we find the extra Gaussian broadening (discussed in Sec. II) to be w_g=0.8 eV in this case. Using this w_g value and the general relation between ΔE_B and bubble radius in Fig. 4, we find the width of the size distribution of the bubble to be ±2 Å.

Turning to Ne $1s_B$, we note that its BE is larger by about 1.2 eV than $1s_A$ at 0.3 keV. This would imply that the beneath subsurface Ne bubbles corresponding to $1s_B$ would have sizable radius even at 0.3 keV and cannot be approximated by the Van der Waals radius. This is not surprising since they occur at considerable depths varying from 20 to 120 Å [Fig. 1(d)]. If the implantation depth is large, the probability of the Ne atoms to backscatter out of the Al surface will be less since more number of diffusion steps would be required for the Ne atoms to reach the surface and desorb.[27] So, most of the Ne atoms will precipitate into bubbles of larger size. Here, we take R_0 for $1s_B$ (where ΔE_B=1.3 eV at E_i=0.3 keV) to be equal to the radius of the Ar bubble (9 Å) that has the same ΔE_B value.[9] From the variation in ΔE_B with E_i, we find the radius of the beneath subsurface Ne $1s_B$ bubbles to be about 20 Å at 5 keV. The width of the distribution is found, as discussed above, to be ±6.5 Å. Thus, we find that the bimodal depth distribution of the Ne bubbles also translates to a bimodal distribution in the bubble sizes with two different mean radii (20±6.5 and 4±2 Å, corresponding to Ne $1s_B$ and $1s_A$ peaks, respectively).

The subsurface bubbles (4 Å radius) are expected to be in solid state for the following reason: x-ray diffraction studies on solid Ne as a function of pressure show that above 48.3 kbar Ne solidifies at room temperature.[28] Assuming the validity of the standard relation between pressure and radius of

a bubble,[29] the pressure experienced by the subsurface bubbles ($R=4$ Å) is calculated to be about 200 kbar. This is larger than the threshold pressure (48.3 kbar) indicating that these bubbles are in solid state. On the contrary, the beneath subsurface bubbles would be in fluid state since the corresponding pressure is 40 kbar. Experimentally, 13 Å Ne bubbles have been reported to be in fluid state by Felde *et al.*[1]

For calculating R for Ne $1s_B$ bubbles, the implicit assumption in finding the value of R_0 is that the dependence of R on BE is similar between the different rare gases. This is indeed shown to be so in Fig. 4, where we plot R with ΔE_B for all the rare gases studied by us (Ar, Xe, and Ne).[8,9] R has been obtained based on the relation $\Delta E_B = \frac{c_1}{R} + c_2$ [Eq. (1) of Ref. 8] for the individual rare gases. c_1 and c_2 are variable fitting parameters, the significance of which is discussed in Ref. 8. Reverting this equation, we get $R = \frac{c_1}{\Delta E_B - c_2}$ that is used to fit the data in Fig. 4 for the solid bubbles and extrapolated for the larger fluid Ne bubbles. Thus, a single expression can describe the R variation with BE for all the rare gases, and the fitting parameter values are c_1 (=3.8) and c_2 (=0.9). While the fit is good for the solid bubbles, the fluid Ne bubbles seem to follow the trend, *albeit* with more scatter. This may be related to the change in BE due to the fluid state.[30] It is also possible that the simple relation given above that holds for small bubbles needs modification for larger bubbles. Indeed, it is clear that the above expression will not hold for $\Delta E_B \leq c_2$, where R becomes unphysical.

Finally, it may be noted that, while the present work establishes and explains the existence of two peaks in Ne 1s for Ne nanobubbles in Al and the quality of the data fitting is good indicating likely absence of more peaks due to our limited resolution, it is possible that finer features in the Ne 1s spectral line shape might have remained undetected. For example, Ne atoms at the Al-bubble interface might have slightly different BE compared to those inside the bubble. So, future experiments using undulator based beamlines in third generation synchrotron sources that provide high photon flux with improved energy as well as spatial resolution will be interesting to perform. For bubbles embedded in the bulk region (depth in order of microns), bulk sensitive high energy photoemission experiments using synchrotron radiation would be useful.

IV. CONCLUSION

The Ne 1s core level for Ne nanobubbles in Al exhibit a double peak structure that changes in relative intensity with the implantation conditions, isochronal annealing, and sputtering. By analyzing these photoelectron spectroscopy data, we conclude that a bimodal depth and size distribution of Ne nanobubbles exists. The smaller sized subsurface bubbles of 4 ± 2 Å radius occur close to the Al surface while the bigger sized bubbles (20 ± 6.5 Å radius) occur deeper beneath the surface. Such a bimodal distribution of bubbles has not been observed for Ar or Xe. By calculating the pressure experienced by the bubbles, we propose that the smaller bubbles are in solid state while the bigger bubbles are in fluid state. We further show that it is possible to estimate the bubble radii for a rare-gas bubble in Al from the core-level binding energy shifts.

ACKNOWLEDGMENTS

We thank J. Fink, A. Chakrabarti, and G. Amarendra for useful discussions. Fundings from the D.S.T.–Max-Planck Partner Group project and Ramanna Research Grant are gratefully acknowledged.

*barman@csr.ernet.in

[1] A. vom Felde, J. Fink, T. Muller-Heinzerling, J. Pfluger, B. Scheerer, G. Linker, and D. Kaletta, Phys. Rev. Lett. **53**, 922 (1984).
[2] C. J. Rossouw and S. E. Donnelly, Phys. Rev. Lett. **55**, 2960 (1985).
[3] S. E. Donnelly, R. C. Birtcher, C. W. Allen, I. Morrison, K. Furuya, M. Song, K. Mitsuishi, and U. Dahmen, Science **296**, 507 (2002).
[4] M. Schmid, W. Hebenstreit, P. Varga, and S. Crampin, Phys. Rev. Lett. **76**, 2298 (1996).
[5] J. E. Inglesfield and J. B. Pendry, Philos. Mag. **34**, 205 (1976).
[6] J. Fink, Adv. Electron. Electron Phys. **75**, 121 (1989).
[7] S. E. Donnelly and C. J. Rossouw, Science **230**, 1272 (1985); Nucl. Instrum. Methods Phys. Res. B **13**, 485 (1986).
[8] C. Biswas, A. K. Shukla, S. Banik, S. R. Barman, and A. Chakrabarti, Phys. Rev. Lett. **92**, 115506 (2004).
[9] R. S. Dhaka, C. Biswas, A. K. Shukla, S. R. Barman, and A. Chakrabarti, Phys. Rev. B **77**, 104119 (2008).
[10] R. S. Dhaka, K. Gururaj, S. Abhaya, G. Amarendra, S. Amirthapandian, B. K. Panigrahi, K. G. M. Nair, N. P. Lalla, and S. R. Barman, J. Appl. Phys. **105**, 054304 (2009).
[11] B. J. Waclawski, J. W. Gadzuk, and J. F. Herbst, Phys. Rev. Lett. **41**, 583 (1978).
[12] R. E. Watson, J. F. Herbst, and J. W. Willkins, Phys. Rev. B **14**, 18 (1976).
[13] P. H. Citrin and D. R. Hamann, Phys. Rev. B **10**, 4948 (1974); Chem. Phys. Lett. **22**, 301 (1973).
[14] C. Biswas, A. K. Shukla, S. Banik, V. K. Ahire, and S. R. Barman, Phys. Rev. B **67**, 165416 (2003).
[15] C. Busse, C. Engin, H. Hansen, U. Linke, T. Michely, and H. M. Urbassek, Surf. Sci. **488**, 346 (2001); C. Busse, H. Hansen, U. Linke, and T. Michely, Phys. Rev. Lett. **85**, 326 (2000).
[16] W. H. Press, S. A. Teukolsky, W. T. Vellerling, and V. P. Flannery, *Numerical Recipes in Fortran* (Cambridge University Press, New York, 1992).
[17] S. Doniach and M. Šunjić, J. Phys. C **3**, 285 (1970).
[18] M. Coreno, L. Avaldi, R. Camilloni, K. C. Prince, M. de Simone, J. Karvonen, R. Colle, and S. Simonucci, Phys. Rev. A **59**, 2494 (1999).
[19] W. Theis and K. Horn, Phys. Rev. B **47**, 16060 (1993).
[20] M. Cardona and L. Ley, *Photoemission in Solids: General Prin-*

ciples (Springer-Verlag, Berlin, 1978).
[21] R. Manzke, G. Crecelius, W. Jager, H. Trinkaus, and R. Zeller, Radiat. Eff. **78**, 327 (1983).
[22] J. P. Biersack and L. Haggmark, Nucl. Instrum. Methods **174**, 257 (1980).
[23] M. Ghaly and R. S. Averback, Phys. Rev. Lett. **72**, 364 (1994).
[24] D. Kaletta, Radiat. Eff. **78**, 245 (1983).
[25] J. C. Rife, S. E. Donnelly, A. A. Lucas, J. M. Gilles, and J. J. Ritsko, Phys. Rev. Lett. **46**, 1220 (1981).
[26] R. Manzke, G. Crecelius, W. Jäger, H. Trinkaus, R. Zeller, and J. Fink, Radiat. Eff. **78**, 327 (1983).
[27] D. J. Reed, Radiat. Eff. **31**, 129 (1977).
[28] L. W. Finger, R. M. Hazen, G. Zou, H. K. Mao, and P. M. Bell, Appl. Phys. Lett. **39**, 892 (1981).
[29] H. Trinkaus, Radiat. Eff. **78**, 189 (1983).
[30] S. R. Barman and D. D. Sarma, Phys. Rev. B **51**, 4007 (1995).